



Two-dimensional Blue-AsP Monolayers with Tunable Direct Band Gap and Ultrahigh Carrier Mobility Show Promising High-performance Photovoltaic Properties

Journal:	<i>Nanoscale</i>
Manuscript ID	NR-ART-02-2019-001261.R1
Article Type:	Paper
Date Submitted by the Author:	18-Mar-2019
Complete List of Authors:	<p>Cai, Xinyong; Southwest Jiaotong University, Chen, Yuanzheng; Southwest Jiaotong University, School of Physical Science and Technology Sun, Bai; Southwest Jiaotong University, School of Physical Science and Technology Chen, Jiao; Southwest Jiaotong University, School of Physical Science and Technology Wang, Hongyan; Southwest Jiaotong University, school of physical science and technology Ni, Yuxiang; Southwest Jiaotong University, School of Physical Science and Technology Tao, Li; Chengdu University of Information Technology Wang, Hui; Southwest Jiaotong University, Zhu, Shou; Southwest Jiaotong University, School of Physical Science and Technology Li, Xiumei; Southwest Jiaotong University, School of Physical Science and Technology, Key Laboratory of Advanced Technologies of Materials, Ministry of Education of China Wang, Yanchao; Jilin University, State Key Laboratory of Superhard Materials Lv, Jian; Jilin University, College of Materials Science and Engineering Feng, Xiaolei; University of Cambridge Redfern, Simon; University of Cambridge, Department of Earth Sciences Chen, Zhongfang; University of Puerto Rico, Department of Chemistry</p>

Two-dimensional Blue-AsP Monolayers with Tunable Direct Band Gap and Ultrahigh Carrier Mobility Show Promising High-performance Photovoltaic Properties

Xinyong Cai,^{a, 1} Yuanzheng Chen,^{a, 1, *} Bai Sun,^{a, c} Jiao Chen,^a Hongyan Wang,^a Yuxiang Ni,^a Li Tao,^b Hui Wang,^{a, c} Shouhui Zhu,^a Xiumei Li,^a Yanchao Wang,^c Jian Lv,^c Xiaolei Feng,^f Simon A.T. Redfern,^f and Zhongfang Chen^{d, *}

^a School of Physical Science and Technology, Key Laboratory of Advanced Technologies of Materials, Ministry of Education of China, Southwest Jiaotong University, Chengdu 610031, China.

^b School of Optoelectronic Technology, Chengdu University of Information Technology, Chengdu 610225, China

^c State Key Lab of Superhard Materials, College of Physics, Jilin University, Changchun 130012, China

^d Department of Chemistry, University of Puerto Rico, Rio Piedras Campus, San Juan, PR 00931, USA

^e Department of Mechanics and Mechatronics Engineering, Centre for Advanced Materials Joining, Waterloo Institute of Nanotechnology, and Department of Physics and Astronomy, University of Waterloo, Waterloo, Ontario N2L 3G1, Canada

^f Department of Earth Sciences, University of Cambridge, Cambridge, CB2 3EQ, UK

¹ These authors contributed equally

Abstract

The successful fabrication of black phosphorene (Black-P) in 2014 and subsequent synthesis of layered Black $\text{As}_{1-x}\text{P}_x$ alloys has inspired research into two-dimensional (2D) binary As-P compounds. The very recent success in growing blue phosphorene (Blue-P) further motivated exploration of 2D blue-AsP materials. Here, using *ab initio* swarm-intelligence global minimum structure-searching methods, we have obtained a series of novel and energetically-favored 2D blue-AsP (denoted x-AsP, x= I, II, III, IV, V) compounds with As:P = 1:1 stoichiometry. They display similar honeycomb structures to Blue-P. Remarkably, the lowest-energy AsP monolayer, namely I-AsP, not only possesses a quasi-direct band gap (2.41 eV) which can be tuned to a direct and optimal gap for photovoltaic applications by in-plane strain, but also has an ultrahigh electronic mobility up to $\sim 7.4 \times 10^4 \text{ cm}^2\text{V}^{-1}\text{s}^{-1}$, far surpassing that of Blue-P, and also exhibits high absorption coefficients ($\times 10^5 \text{ cm}^{-1}$). Our simulations also show that 30 nm-thick I-AsP

sheets-based cells have photovoltaic efficiency as high as $\sim 12\%$, and the I-AsP/CdSe heterostructure solar cell possess a power conversion efficiency as high as $\sim 13\%$. All these outstanding characteristics suggest I-AsP sheet as a promising materials for high-efficiency solar cells.

Introduction

Phosphorus (P) can form various allotropes in the bulk, including black P, white P, violet P, and red P, due to inequivalent sp^3 orbital hybridization.^{1,2} Very recently, a two-dimensional (2D) black P, *i.e.* phosphorene (Black-P), has been successfully synthesised, and is found to display a high electron mobility of $\times 10^4$ cm²/V/s with a direct band gap of ~ 2 eV.^{3,4} This great achievement inspired the discovery of a series of allotropes, such as β -, γ -, δ -, ϵ -, ζ -, η -, θ -, ψ -, the octagonal tiling, tricycle-like phosphorene, and blue phosphorene (Blue-P).⁵⁻¹³ Among these 2D allotropes, blue-P is probably most appealing due to its theoretically-predicted wide tunable direct-bandgap (1.1 eV \sim 2 eV), enhanced by in-layer strain and the number of layers¹⁴ and isotropic structure. Unlike the anisotropic structure of Black-P, the in-plane hexagonal unit of Blue-P possesses isotropic structure and properties, and its bulk layer stacking is very similar to graphite. Remarkably, Blue-P has been successfully synthesized on an Au (111) substrate by molecular beam epitaxy,¹⁵ as well as on tellurium functionalized Au(111) using black P as the precursor.¹⁶ However, Blue-P exhibits rather low carrier mobility of $\times 10^2$ cm²/V/s,¹⁷ which restricts its application as a photoelectric device material.

Arsenic (As), having a similar covalent radius as P among the group V elements, also exists as crystalline allotropes including black As and gray As.² Black As is isostructural with black P, while gray As resembles blue P. Their limited layers make them promising candidates for photoelectric applications, as supported by both theoretical¹⁸⁻²⁴ and experimental²⁵ studies. Moreover, other As allotropes, including honeycomb structured γ -As, T-As and δ -As, are all predicted to have excellent photoelectric and thermoelectric performance.²⁶⁻²⁹ Among these allotropes, gray As is thermodynamically most favored, and its multilayer nanoribbons have been synthesized via InAs.^{17, 27, 30} Due to its low interlayer interaction energy,³¹ it is rather easy to mechanically exfoliate gray As bulk to produce monolayer gray arsenene (Gray-As), which was

recently predicted to be a semiconductor with a wide band gap (~ 2.5 eV)³² with high carrier mobility for optoelectronic applications.²⁹

Considering the identical 2D configuration of black-, blue-P and -As (with its exceptional properties), 2D binary black As-P and blue As-P phases provide a means to develop new materials with modulated optoelectronic properties, including improved carrier mobility. The recent success in synthesizing a limited-layer black $\text{As}_{1-x}\text{P}_x$ ($0.17 \leq x \leq 1$) alloy, a promising alternative material for mid-infrared applications,^{18, 33-36} lends confidence to attempts to fabricate such 2D binary materials. Meanwhile, other 2D As-P structures, mainly with As:P = 1 :1 stoichiometry, such as α -AsP, β -AsP, γ -AsP, ε -AsP, δ -AsP, have also been proposed as promising optoelectronic materials.³⁷⁻³⁹ However, these AsP polymorphs were obtained by simply replacing alternative P atoms by As atoms.

Here, to further explore 2D binary As-P compounds, we have systemically investigated the low-lying energy structures of As-P monolayer phases ($\text{As}_x\text{P}_{1-x}$, $x = 1/6, 1/5, 1/4, 1/3, 1/2, 1/3, 1/4, 1/5$, and $1/6$) using the particle-swarm optimization (PSO) multidimensional method⁴⁰. As such, we confirm the high stability of the As:P = 1:1 composition, and have obtained a series of novel and energetically-favorable 2D blue AsP monolayers sharing similar honeycomb structure to Blue-P and Gray-As at this composition. More importantly, the most stable I-AsP monolayer possesses a tunable direct bandgap, high absorption coefficients, ultrahigh carrier mobility, and superior photovoltaic efficiency. Compared with Blue-P, the properties of I-AsP are greatly enhanced by As merging, and some aspects are close to or even beyond those of Gray-As, suggesting Blue-AsP is a promising material for photovoltaic applications. By following a type II band alignment, we have constructed a novel solar cell comprising a I-AsP/CdSe heterostructure, and further demonstrate a relatively high conversion efficiency of $\sim 13\%$ in these cells.

Computational methods

By means of the multidimensional particle-swarm optimization (PSO) method implemented in the CALYPSO code^{40, 41}, we searched for low-lying structures of 2D $\text{As}_x\text{P}_{1-x}$ monolayer ($x = 1/6, 1/5, 1/4, 1/3, 1/2, 1/3, 1/4, 1/5$ and $1/6$). The validity of this method has been proved by various systems ranging from elemental to binary and ternary compounds and from the ground-state structures of 3D crystals to clusters and 2D crystals.⁴²⁻⁴⁸ The geometric optimizations and

electronic properties computations for the 2D As-P structures were performed using Perdew–Burke–Ernzerhof (PBE) functional in the density functional theory (DFT) framework within the generalized gradient approximation (GGA) and projector-augmented-wave (PAW),^{49, 50} as implemented in the Vienna ab initio simulation package (VASP).⁵¹ A vacuum space of 20 Å was used to avoid mirror interactions of adjacent As-P freestanding monolayers. The van der Waals density functional⁵² was adopted to evaluate interlayer interactions more accurately. A Monkhorst-Pack k meshes (the reciprocal space was set to be $0.025 \times 2\pi \text{ \AA}^{-1}$) were selected for Brillouin zone sampling to insure that all energy calculations are well converged to ~ 1 meV. The Heyd–Scuseria–Ernzerhof (HSE) hybrid functional⁵³ was employed to evaluate the electronic band structures. The dynamic stability of the 2D blue AsP monolayers was verified through the direct supercell method, as implemented in the PHONOPY code.⁵⁴ The ab initio molecular dynamics (AIMD) simulations were annealed at 300 and 750K in NVT ensemble, which lasted for 7.5 ps with a time step of 2.0 fs.

Results and discussions

Structures and stabilities of blue-AsP monolayer

Both P and As are Group V elements, and can give rise to sp^3 hybridization. The covalent atomic radius of As is very close to that of P (covalent radii: 1.00 and 1.15 Å, respectively), thus the binary As-P compositions most easily form 2D crystalline structures like Black-P (Black-As) and Blue-P (Gray-As).

Based on our CALYPSO approach with the first principles calculations, we comprehensively explored various possible monolayers with different As-P stoichiometries. By computing the formation energies and plotting the convex hull (Figure S1), we found that the energy differences between different compositions are exceedingly small, indicating that the As-P system may form an alloy. Among these stoichiometries, the As:P = 1:1 composition is thermodynamically most favorable in the 2D space. With this 1:1 composition, besides finding several typical monolayer AsP polymorphs (α , β , γ , δ , and ϵ), we also found a series of novel AsP monolayers (label as x -AsP, x = I, II, III, IV, V), and their structural parameters are given in Table S1. To evaluate the relative stabilities of these monolayers, we computed their cohesive energies ΔE (AsP), defined as $\Delta E(\text{AsP}) = E(\text{AsP}) - E(\text{As}) - E(\text{P})$, where $E(\text{As/P})$ represents the free energy of single P or As

atom, and $E(\text{AsP})$ is that of a AsP monolayer. According to this definition, a more negative $\Delta E(\text{AsP})$ value indicates the higher thermodynamic stability.

Our newly predicted I-AsP is thermodynamically most favorable, especially: it is lower in energy than β -AsP, the previously reported lowest-energy structure (Figure 1a).^{37, 38, 55, 56} Moreover, the cohesive energies of II-, III-, IV-, and V-AsP all are close to that of β -AsP, and much lower than that of α -AsP (Figure 1b). In these x-AsP structures, both P and As atoms are three-fold coordinated with sp^3 hybridization, forming buckled honeycomb hexagonal units.

Viewing these x-AsP structures from above (down onto the layers, Figure 1c), we notice that these honeycomb x-AsP structures share extreme similarity with the atomic arrangement of Blue-P⁵⁷ (or Gray-As³², Figure 1c). Viewed parallel to the layers, the puckered zigzag of these x-AsP structures in the cross-section significantly differs from the distinct armchair ridges of Black-P (or black AsP such as α -AsP, Figure 1b) that causes the anisotropy of Black-P, which is also similar to the puckering of Blue-P (Gray-As). Thus, these x-AsP sheets can be characterized by a combined structure of Blue-P and Gray-As, which we denote “blue AsP”. Among these x-AsP sheets, the I-AsP is thermodynamically most stable, and is expected to be most readily achieved by experimental synthesis. Thus, in the following sections, we will focus on the I-AsP sheets.

The I-AsP monolayer contains two different hexagonal units, one consists of three neighbouring As and P atoms, and the other has three alternated As and P atoms. The unit cell consists of six atoms with lattice constants $a = b = 5.96 \text{ \AA}$. In the puckered structure, there are three types of bonds with bond lengths $d_1 = 2.52 \text{ \AA}$ of As-As, $d_2 = 2.25 \text{ \AA}$ of P-P, and $d_3 = 2.40 \text{ \AA}$ of As-P, and four types of bond angles: $\theta_1 = 94.1^\circ$, $\theta_2 = 90.9^\circ$, $\theta_3 = 95.6^\circ$ and $\theta_4 = 89.2^\circ$ (Figure 1c).

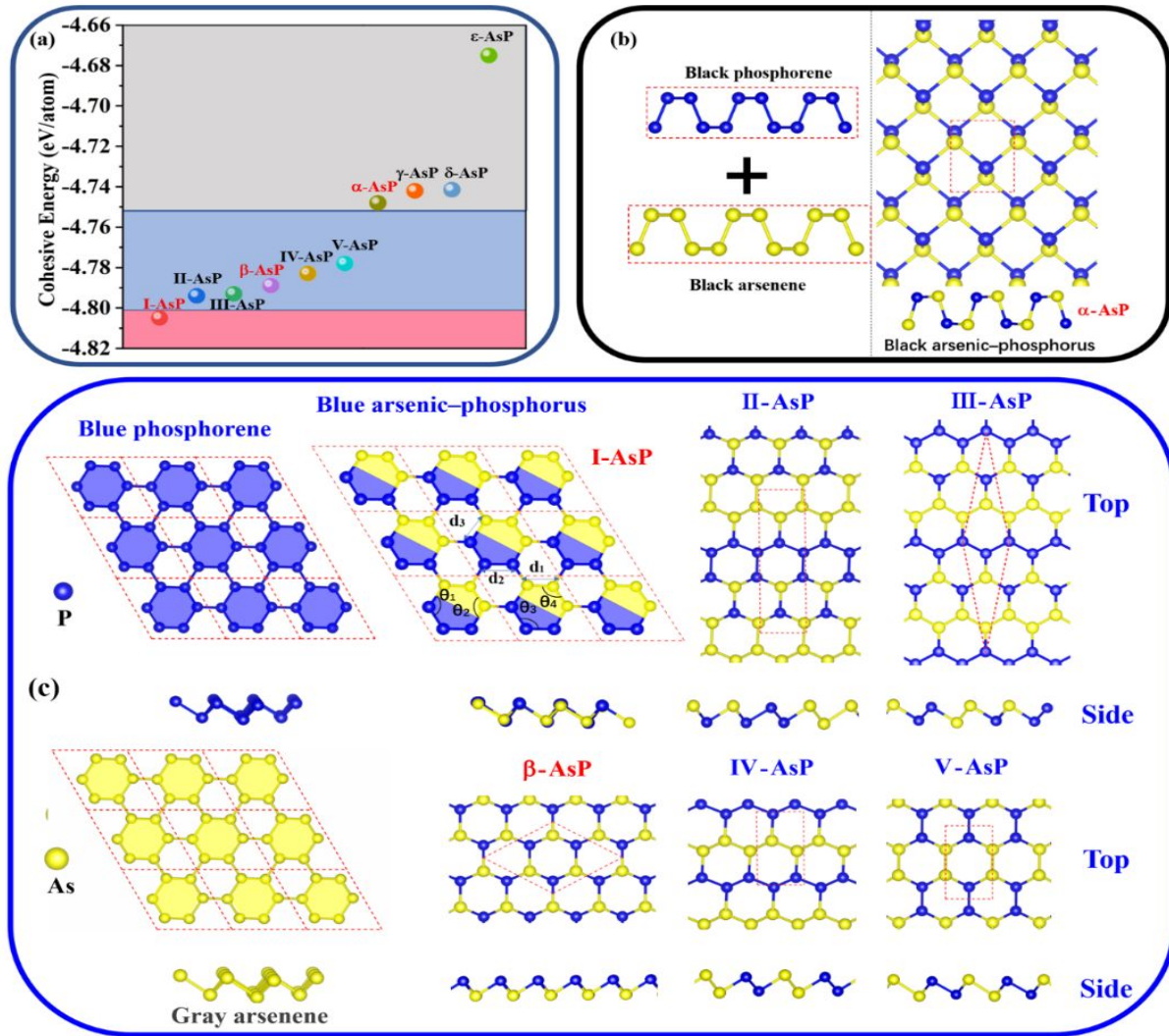


Figure 1. (a) The computed cohesive energies of our newly predicted x -AsP ($x = \text{I, II, III, IV, V}$) monolayers in comparison with those of typical AsP polymorphs ($\alpha, \beta, \gamma, \delta,$ and ϵ). (b) The side and top views of α -AsP as a combined structure of Black-P and Black-As. (c) The side and top views of Blue-P, Gray-As, β -AsP, and our newly predicted I-, II-, III-, IV-, and V-AsP monolayers.

To evaluate the dynamic stability of I-AsP monolayer, we calculated its phonon dispersion relations using the finite-displacement method. No imaginary frequency in the first Brillouin zone was found (Figure 2a), which confirms its dynamic stability. Moreover, the thermal stability of I-AsP was examined by AIMD simulations. For $T = 300$ K, the I-AsP monolayer

only undergoes a minimal change, and no remarkable structural disruption is observed throughout simulations. Meanwhile, we performed AIMD simulations at 300 K in an O₂ atmosphere (Figure S2). After full atomic relaxation over a run of 7.5 ps, the I-AsP structure obtained from AIMD simulations at 300 K retains its initial configuration without any sign of oxidation. These simulations demonstrate that I-AsP monolayer is stable at room temperature. When the temperature increases up to 750 K, the monolayer structures start to break down and gradually lose their structure integrity (Figure S2).

Significantly, adopting an alloying strategy, recent experiments have synthesized limited-layer black As_{1-x}P_x alloys with different and tunable compositions ($0.17 \leq x \leq 1$) at elevated temperatures.^{18, 19} We are aware that the experimental synthesis of black As_{1-x}P_x alloys is largely affected by temperature.⁵⁸ Since our AIMD simulations suggest that I-AsP is not stable at 750 K, we followed a different route to prepare I-AsP in this study. Very recently, Cui *et al.*⁵⁹ proposed a novel kinetic pathway for fabricating Blue-P via epitaxial growth; Zhang *et al.*¹⁵ experimentally realized a molecular beam epitaxial growth of Blue-P on Au(111) by using black P as precursor. Meanwhile, Chen *et al.*¹⁶ successfully grew quasi-free-standing Blue-P on the Te-functionalized Au(111). These remarkable experimental achievements pave a way to the synthesis for the Blue-AsP (I-AsP).

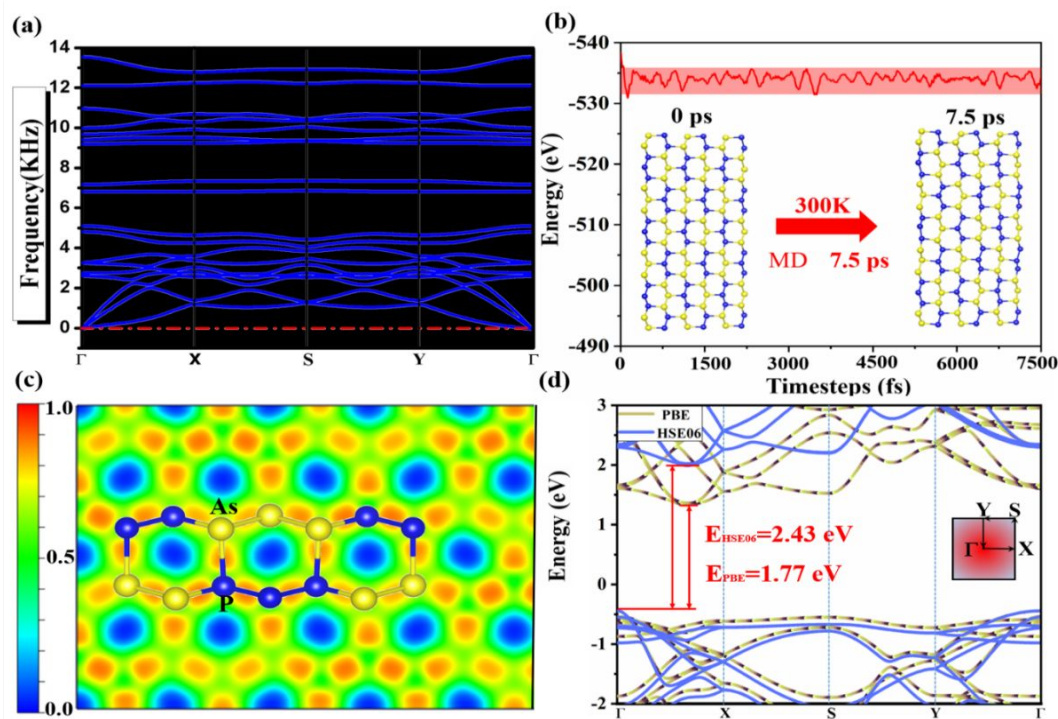


Figure 2. (a) The calculated phonon spectrum for the I-AsP monolayer, (b) the evolution of total energy and the structures of I-AsP monolayer from AIMD simulations at T=300 K, (c) ELF maps sliced perpendicular to the (001) direction for the I-AsP monolayer, and (d) the electronic band structures of the I-AsP monolayer at PBE and HSE06 levels of theory. High symmetry k points in the first Brillouin zone: Γ (0, 0, 0), X (0.5, 0, 0), S (0.5, 0.5, 0) and Y (0, 0.5, 0).

Electronic properties and tunable bandgap engineering

To understand the chemical bonding, the electron localization function (ELF) and the corresponding partial densities of states (DOS) of I-AsP monolayer were calculated. In the ELF (Figure 2c), abundant electrons are tightly localized between adjacent atoms, revealing the strong covalent electron states of the σ bond formed by the sp^3 -hybridized orbitals of As and P atoms. The calculated DOS of I-AsP monolayer (Figure S3) has strongly overlapping s-p orbitals for As and P atoms, confirming these covalent bonding characters.

The I-AsP monolayer is semiconducting with a quasi-direct band gap (Figure 2d). The valence band maximum (VBM) occurs at the Γ point, while the conduction band minimum (CBM) lies between the Γ and X points, and is only slightly higher in energy than the Γ point. Such a weak indirect-bandgap is advantageous for photovoltaic applications (seeing below), and also permits strong absorption and high electron mobilities, as reported in the InP₃ monolayer and some hybrid perovskites.^{60, 61} Particularly, the bandgap of the I-AsP monolayer (1.77 eV at PBE and 2.41 eV at HSE06) is well-suited to photovoltaic applications.

Compressive or tensile strains have been demonstrated, both experimentally and theoretically, as an effective method to modulate the electronic band structures.⁶² Meanwhile, 2D materials can easily bear a certain strain effect, which can be operated through a lattice mismatch on a substrate or by mechanical loading in experiments.²⁰ Therefore, we have examined the effect of strain on the band structures of I-AsP monolayer. An imposed uniaxial strain is defined as $\delta = \Delta l/l_0$, where Δl is the change of the lattice constant and l_0 is the lattice constant of the rectangle supercell. Dependence of the band gap on the in-plane stretching along zigzag direction and armchair direction was calculated under strain from -15 % to 15 % (Figure 3a), respectively. Interestingly, the band gaps of the I-AsP monolayer decrease gradually with either compressive or tensile strains, which differs from the monotonic trend from compression to tension as found

in the case of Black-P.³ This feature can be attributed to Mexican-hat-like⁶³ flat valence bands, which render sharp peaks in the density of states (DOS) and van Hove singularities (VHSs) with $\frac{1}{\sqrt{E}}$ divergence near the Fermi level as suggested by Figure S3, akin to Blue-P¹⁴ and InP3 monolayers⁶⁴. Such electronic states bring about a non-monotonic response of the VBM or CBM to various strains and lead to unusual band-gap trend from compression to tension.

Moreover, the structures of monolayer I-AsP can change into multilayer by a van der Waals (vdW) stacking strategy. The possible stacking patterns for bilayer (2L) and trilayer (3L) I-AsP are presented in Figure S4 and their cohesive-energy differences are evaluated (Table S2-S3). Among, the AB and ABC stacking are the ground state structures, which is the same as the Blue-P and Gray-As. Adopting the stable 2L (AB) and 3L (ABC) stackings, we further calculated the layer-dependent bandgap of I-AsP sheets (Figure 3b). We found that the bandgap of I-AsP can also be tuned by increasing the number of layers, and shows a monotonic decrease with increasing the I-AsP layers.

Interestingly, the band gap on the in-plane stretching along zigzag direction direction and biaxial strain can be tuned to have direct character (Figure S5). The I-AsP monolayer has an indirect-to-direct gap transition at the Γ point under tensile strains of $\sim 13\%$ along zigzag direction (Figure 3c) and under $\sim 3.8\%$ biaxial compressive strain (Figure 3d), respectively. Notably, the character of direct band gap can be fixed and the gap value changed from ~ 0 eV to ~ 2 eV by biaxial strain from 3.8% to 6% under PBE level (Figure S5). These bandgap characteristics for the I-AsP monolayer, in response to tensile strains, are quite similar to those of Blue-P and Gray-As.¹⁴ Such strain-tuned direct band gap has a clear advantage for its potential photovoltaics applications, as electronic excitation becomes possible at lower phonon energy.

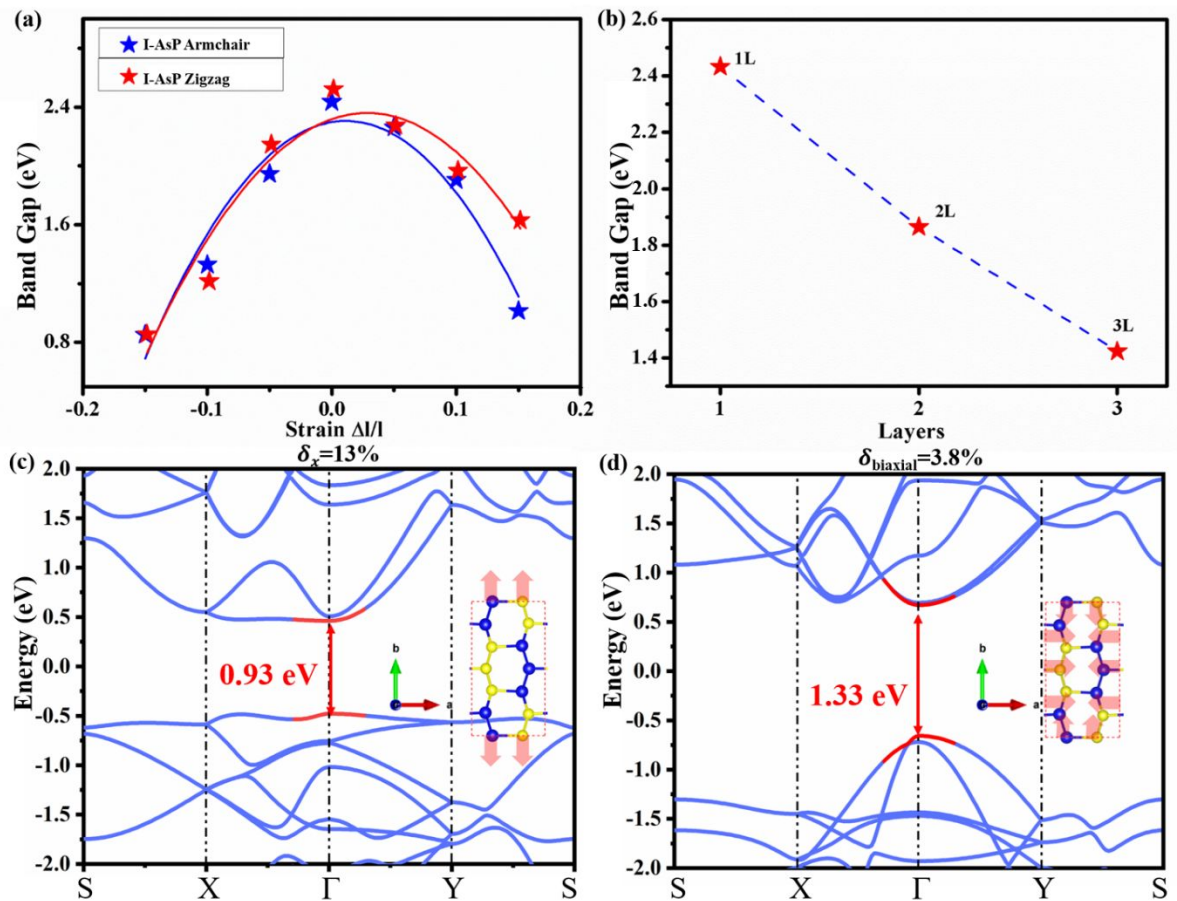


Figure 3. (a) Dependence of the band gap of I-AsP monolayer on the in-layer strain from -15% to 15%, (b) the layer-dependent bandgap of I-AsP. (c-d) The indirect-direct semiconductor transition is triggered by 13% tensile strain along zigzag direction (c) and 3.8% biaxial compressive strain (d), respectively.

Carrier mobilities of I-AsP monolayer

We note that the conduction bands in the calculated band structure of I-AsP monolayer are rather dispersive, which implies a high electron mobility. Thus, we have theoretically investigated the carrier mobilities of the I-AsP monolayer along the zigzag and armchair directions. According to the deformation potential (DP) proposed by Bardeen and Shockley,⁶⁵ under the effective mass (m^*) approximation, the analytical expression of acoustic-phonon-limited carrier mobility (μ) in 2D materials is given as

$$\mu = \frac{e\hbar^3 C_{2d}}{k_B T m^* m_d (E_{2d}^*)^2}$$

in which k_B is the Boltzmann constant, e is the electron charge, and the temperature T is set to be 300 K. The average effective mass (m_d) is equal to $m_d = \sqrt{m^a m^b}$. The effective mass m^* (m^a , m^b) of holes and electrons are calculated based on the data about the band structure (VBM for holes and CBM for electrons along Γ -X and Γ -Y for the rectangle cell) is given by the equation:

$$m^* = \hbar^2 \left[\frac{\partial^2 E(k)}{\partial k^2} \right]^{-1}$$

where k is the wave vector, and $E(k)$ is the energy corresponding to k . The $C_{2d} = [\partial^2 E / \partial \delta^2] / S_0$ and $E_{2d}^* = \partial \Delta E / \partial \delta$ are the in-plane stiffness with the longitudinal strain and the deformation potential as the change of band edges in VBM for holes and CBM for electrons when in-plane strains are employed along the zigzag and armchair directions, respectively. And S_0 and ΔE are the area of the equilibrium supercell and the value of CBM (VBM) relative to the vacuum energy, respectively. $\delta = \Delta l / l_0$, and E is the total energy.

Related data are given in Figure S6. The calculated deformation potential constant E_{2d}^* , the elastic modulus C_{2d} , the effective mass m^* and mobility μ of electrons and holes along zigzag and armchair directions are summarized in Table 1. Except for the 2D elastic modulus C , most quantities are of moderate magnitudes and are anisotropic along the zigzag and armchair directions. These features are rather similar to Blue-P and Gray-As: the directional 2D elastic modulus C for the I-AsP, Blue-P, and Gray-As all are relatively isotropic, which may result from their similar planar isotropic hexatomic rings. Comparing the calculated m^* values for I-AsP, Blue-P, and Gray-As, the effective mass m^* of electrons are within an order of magnitude, but are smaller than the corresponding value for holes, which can be understood by the very flat valence band and more dispersive conduction band. As expected, the distinctively dispersive conduction bands lead to ultrahigh electronic mobility in both zigzag and armchair directions. The calculated electron mobility for I-AsP monolayer is up to $\sim 7.4 \times 10^4 \text{ cm}^2 \text{V}^{-1} \text{s}^{-1}$, which far surpasses that of Blue-P ($\sim 4.7 \times 10^2 \text{ cm}^2 \text{V}^{-1} \text{s}^{-1}$),¹⁷ Gray-As ($\sim 4.74 \times 10^3 \text{ cm}^2 \text{V}^{-1} \text{s}^{-1}$),²⁹ and the α -AsP ($\sim 1.4 \times 10^4 \text{ cm}^2 \text{V}^{-1} \text{s}^{-1}$),³⁸ and suggests its ability for high charge carrier transfer in photovoltaics applications. Moreover, the carrier mobilities of bilayer and trilayer I-

AsP were evaluated (Table S4). Our calculations indicate that μ strongly depends on the number of layers and are anisotropic in the zigzag (x) and armchair (y) directions. Electron mobilities in the x direction and holes mobility along the x or y direction are increasing with the number of layers, which was expected already from the change of effective mass and deformation potential constant in their band structure (Figure S8-S9).

Table 1. Calculated effective mass (m^*/m_0), deformation potential constant (E_d), 2D elastic modulus C^{2D} , and mobility (μ) for electron (e) and holes (h) along zigzag (y) and armchair (x) directions.

2D structures		m_x^*/m_0	m_y^*/m_0	C_x^{2D} (Nm ⁻¹)	C_y^{2D} (Nm ⁻¹)	E_d^x (eV)	E_d^y (eV)	μ_x cm ² V ⁻¹ s ⁻¹	μ_y cm ² V ⁻¹ s ⁻¹
I-AsP 10 ³	e	0.11	0.12	62.51	63.18	2.30	1.08	17.50×10^3	$74.49 \times$
	h	0.10	0.46	62.51	63.18	10.18	2.13	540	2550
Gray-As ^a 10 ³	e	0.13	0.13	55.50	55.50	3.9	3.9	4.74×10^3	$4.74 \times$
	h	0.53	0.53	55.50	55.50	1.7	1.7	1460	1460
Blue-P ^b	e	0.94	0.14	78.09	78.19	3.20	2.09	4.7×10^2	50
	h	3.48	0.83	78.09	78.19	0.61	11.85	1710	60

^a Ref. 29.; ^b Ref. 17.

Optical properties of I-AsP monolayer

We have calculated absorption properties based on the dielectric function $\varepsilon(\omega) = \varepsilon_1(\omega) + i\varepsilon_2(\omega)$, where ω is the frequency. The absorption coefficient $\alpha(\omega)$ was calculated from

$$\alpha(\omega) = \sqrt{2}\omega(\sqrt{\varepsilon_1^2(\omega) + \varepsilon_2^2(\omega)} - \varepsilon_1(\omega))^{1/2}$$

where ε_1 is the real part of complex dielectric function, which could be obtained from ε_2 using the Kramer–Kronig relationship. The ε_2 is defined as:^{5,6}

$$\varepsilon_2(\omega) = \frac{4\pi^2 e^2}{\Omega} \lim_{q \rightarrow 0} \frac{1}{q^2} \sum_{c,v,k} 2w_k \delta(\varepsilon_{ck} - \varepsilon_{vk} - \omega) \\ \times \langle \mu_{ck + e_\alpha} | \mu_{vk} \rangle \langle \mu_{ck + e_\beta} | \mu_{vk} \rangle^*$$

where α and β refer to x and y directions, and Ω is the volume of the unit cell. The indices c and v refer to the conduction and valence band states, respectively. μ_{ck} corresponds to an eigenstate with wave vector k .

We have calculated the absorption coefficients of I-AsP and compared them with those of Blue-P and Gray-As (Figure 4a). The overall absorption coefficients along in-plane directions (zigzag direction and armchair) of the I-AsP monolayer are larger (10^5 cm^{-1}) than those of Blue-P, and comparable to those of Gray-As. Their absorption coefficients along zigzag and armchair directions are nearly equal for every light region. This relatively isotropic in-plane directional absorption coefficients reflect their planar and rather isotropic strings in the structure. These outstanding optical performances of the I-AsP monolayer suggest that it may be a very promising material for efficient photovoltaic solar cells applications or in optoelectronic devices.

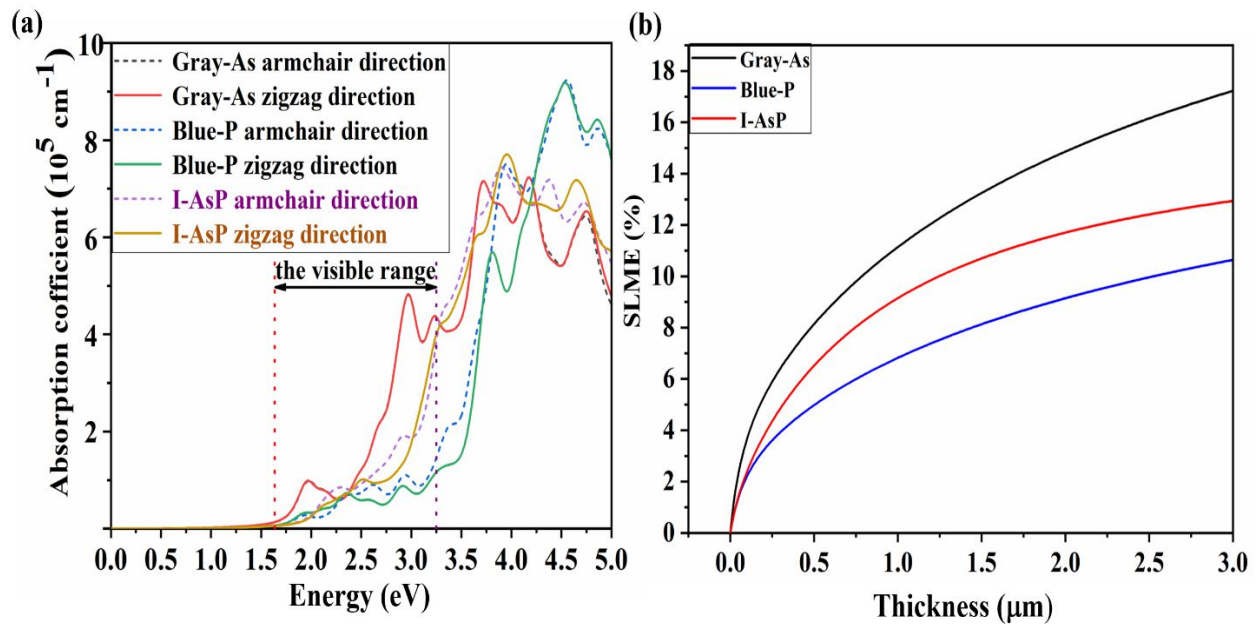


Figure 4. (a) The calculated light absorption spectra for the Gray-As, Blue-P, and the I-AsP monolayer. (b) The theoretical photovoltaic efficiency (SLME) as a function of slab thickness for the I-AsP sheets compared with Gray-As and Blue-P.

The I-AsP sheets as a photovoltaic material in solar cell

The above calculations show that our newly-predicted I-AsP monolayer has a quasi-direct band gap (2.41 eV) similar to that of Blue-P (~2.62 eV) and Gray-As (~2.49 eV), and the quasi-direct band gap is tunable to a direct and optimal gap for photovoltaic applications. The outstanding optical properties further suggest its promise as an efficient photovoltaic material for use in solar cells. Note that the photovoltaic efficiency in the practical solar cells also relies on the thickness of the I-AsP sheets. Thus, we theoretically calculated the photovoltaic efficiencies of the I-AsP sheets, by calculating the spectroscopic limited maximum efficiency (SLME) based on the improved Shockley-Queisser model.⁶⁶ This was done as a function of the thickness by noting the absorption coefficients and the thickness of the sheets. This simulation was performed under the standard AM1.5G solar spectrum at room temperature, and compared with those of Blue-P and Gray-As.

Notably, the SLME of I-AsP sheets are higher than those of Blue-P and close to that of Gray-As for any given thickness (Figure 4b). Their photovoltaic efficiency generally increases as the thickness of these sheets is augmented over the 0~3.0 μm range. For example, 30 nm-thick I-AsP sheets-based cells can have a photovoltaic efficiency up to ~ 12 %, higher than the Blue-P, and comparable to that of c-Si⁶⁷ (~ 10%).

Further, we constructed a type-II band solar cell of I-AsP/CdSe heterostructure (Figure 5a), where I-AsP and CdSe are donor materials and acceptor materials (Figure 5b), respectively, based on the CBM (-4.02 eV) and the VBM (-5.79 eV) for I-AsP as well as the CBM (-4.32 eV) and the VBM (-6.12 eV) for CdSe⁶⁸ (Figure 5c). Subsequently, the energy conversion efficiency (PCE) η of I-AsP/CdSe heterostructure is calculated according to:⁴⁹

$$\eta = \frac{J_{SC}V_{OC}\beta_{FF}}{P_{solar}} = \frac{0.65(E_g^d - \Delta E_c - 0.3) \int_{E_g^d}^{\infty} P(h\omega) d(h\omega)}{\int_0^{\infty} P(h\omega) d(h\omega)}$$

in which J_{sc} , V_{oc} , β_{FF} and P_{solar} are the short circuit current, the maximum open circuit voltage in eV units, the band-fill factor ($\beta_{FF}=0.65$), and the incident solar ($P_{solar}=1000 \text{ Wm}^{-2}$), respectively. Detailedly, J_{sc} is the integral $\int_{E_g^d}^{\infty} P(\hbar\omega) d(\hbar\omega)$ in the limit of 100% external quantum efficiency (EQE)⁶⁹, P_{solar} is obtained from the integral $\int_0^{\infty} P(\hbar\omega) d(\hbar\omega)$ for the AM1.5 solar flux $P(\hbar\omega)$

(stated in $\text{Wm}^{-2} \text{eV}^{-1}$), and V_{oc} is derived from the $(E_g^d - \Delta E_c - 0.3)$ term, where E_g^d is the bandgap of the donor I-AsP, ΔE_c is the energy difference between CBs of the donor I-AsP and the acceptor CdSe.

As can be seen in Figure 5d, the I-AsP/CdSe heterostructure solar cell can possess a PCEs as high as $\sim 13\%$, which is much higher than the best value ($\sim 9\%$) of existing solar cells,⁷⁰ and competitive with the nanocarbon-based photovoltaics ($9\text{--}13\%$),⁷¹ and close to the g-SiC₂ systems ($12\text{--}20\%$),⁷² and the recently proposed MoS₂/ phosphorene heterostructure ($16 \sim 18\%$).^{73,74} These simulations confirmed that the I-AsP sheets can be used as a photovoltaic material in solar cell with a superior photovoltaic efficiency.

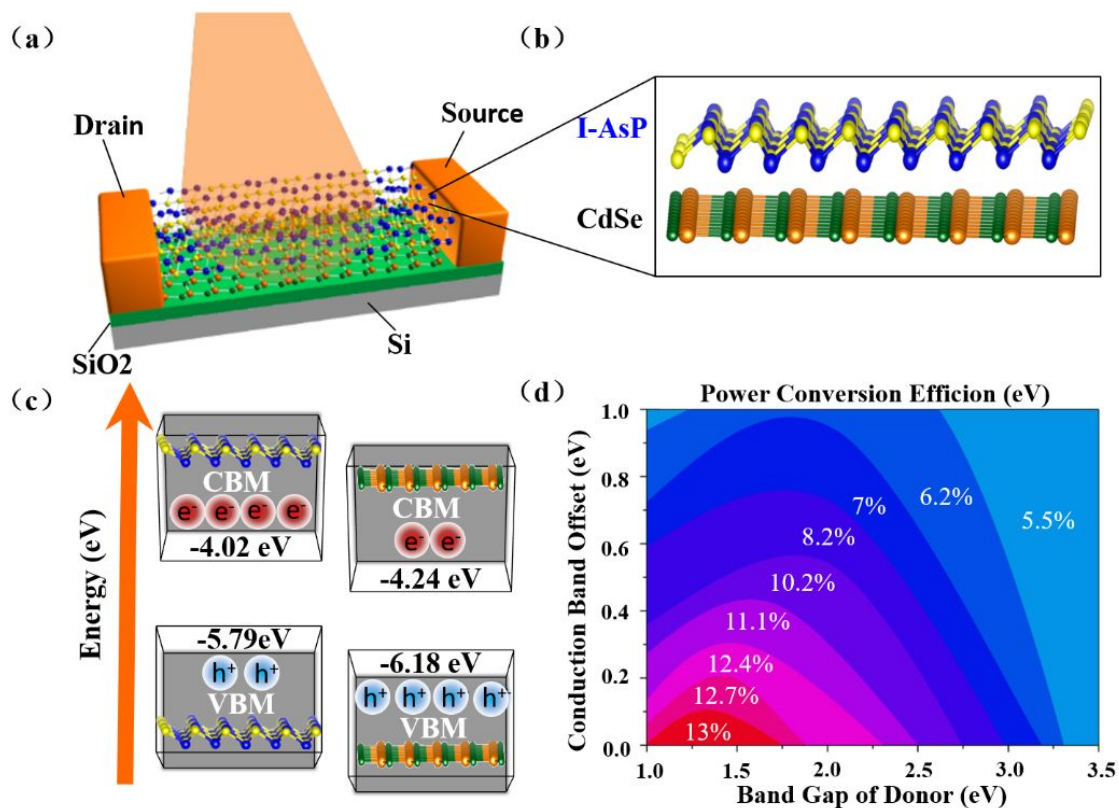


Figure 5. (a) Schematic of the I-AsP/CdSe heterostructure-based solar cell. (b) The optimized structure of the I-AsP/CdSe heterostructure. (c) Schematic drawing of type-II band I-AsP/CdSe heterostructure. (d) Simulated PCE of the heterostructure made by I-AsP/CdSe materials.

Conclusion

In summary, we have identified the low-lying energy structures of the $\text{As}_x\text{P}_{1-x}$ monolayer in 2D space based on the PSO algorithm approach combined with *ab initio* calculations, and confirmed that the As:P = 1:1 composition is thermodynamically most favorable among all the examined stoichiometries. At this 1:1 composition, a series of energetically-favored Blue-AsP monolayers (x -AsP, x = I, II, III, IV, V), sharing similar honeycomb structures with Blue-P, were predicted for the first time. The lowest-energy I-AsP monolayer has a quasi-direct band gap (2.41 eV) and Mexican-hat like flat bands near the Fermi energy, which lead to a nonmonotonic electronic response to compressive and tensile strains. Remarkably, an indirect-to-direct gap transition can occur under tensile strains of $\sim 13\%$ along the zigzag direction or at $\sim 3.8\%$ biaxial compressive strain. Moreover, the I-AsP monolayer possesses extraordinary electronic mobility up to $\sim 7.4 \times 10^4 \text{ cm}^2\text{V}^{-1}\text{s}^{-1}$, and absorption coefficients ($\times 10^5 \text{ cm}^{-1}$) far surpassing those of Blue-P across the entire visible solar spectrum. These advantages demonstrate it as a very promising material for high-efficiency solar cells. As indicated by our simulations, 30 nm-thick I-AsP sheets-based cells can have a photovoltaic efficiency up to $\sim 12\%$, the I-AsP/CdSe heterostructure solar cell can possess a PCEs as high as $\sim 13\%$. All these data strongly suggest that the I-AsP sheets is a very promising photovoltaic material for use in solar cells.

Conflicts of interest

There are no conflicts to declare.

Author Information

Corresponding Authors

*E-mail: (Y. C.) cyz@calypso.org.cn

*E-mail: (Z. C.) zhongfangchen@gmail.com

Notes

The authors declare no competing financial interest.

Author Contributions

Yuanzheng Chen and Zhongfang Chen conceived and designed this work; Xinyong Cai, Jiao Chen, and Xiumei Li performed the related calculations; Xinyong Cai, Shouhui Zhu, and Li Tao prepared the Figure; Bai Sun, Hongyan Wang, Yuxiang Ni, Hui Wang, Yanchao Wang, and Jian Lv gave important discussion; The manuscript was written by Yuanzheng Chen and Zhongfang Chen; Xiaolei Feng and Simon A.T. Redfern discussed related results and reviewed the manuscript. All authors approved the final version of the manuscript.

Supplementary information available

The convex hull for the formation energies for the different As-P stoichiometries; The optimized structural parameters of monolayer x-AsP polymorphs; The AIMD and DOS of the I-AsP monolayer; The dependence of the fundamental band gap for the I-AsP monolayer, bilayer, and trilayer on the in-plane stretching along armchair direction, zigzag direction, and biaxial strain by PBE level; The relationship between energy shift of the band edge position and the dilation Δ/l , total energy shift on per surface as a function of lattice deformation along armchair and zigzag directions.

Acknowledgements

This work was supported in China by the National Natural Science Foundation of China (No. 11604270, 11704050), the Fundamental Research Funds for the Central Universities (2682017CX052; 2018GF08), and the Sichuan Science and Technology program (2017JY005), and in USA by NSF-CREST Center for Innovation, Research and Education in Environmental Nanotechnology (CIRE2N) (Grant Number HRD-1736093). S.A.T.R. acknowledges the support of the UK Natural Environment Research Council under grant NE/P012167/1.

References

1. R. Hultgren, N. S. Gingrich and B. E. Warren, *J. Chem. Phys.*, 1935, **3**, 351-355.
2. S. Zhang, S. Guo, Z. Chen, Y. Wang, H. Gao, J. Gomez-Herrero, P. Ares, F. Zamora, Z. Zhu and H. Zeng, *Chem. Soc. Rev.*, 2018, **47**, 982-1021.
3. H. Liu, A. T. Neal, Z. Zhu, Z. Luo, X. Xu, D. Tománek and P. D. Ye, *ACS Nano*, 2014, **8**, 4033-4041.

4. H. O. Churchill and P. Jarillo-Herrero, *Nat. Nanotechnol.*, 2014, **9**, 330-331.
5. M. Wu, H. Fu, L. Zhou, K. Yao and X. C. Zeng, *Nano Lett.*, 2015, **15**, 3557-3562.
6. J. Guan, Z. Zhu and D. Tomanek, *Phys. Rev. Lett.*, 2014, **113**, 226801.
7. H. Wang, X. Li, Z. Liu and J. Yang, *Phys. Chem. Chem. Phys.*, 2017, **19**, 2402-2408.
8. G. Schusteritsch, M. Uhrin and C. J. Pickard, *Nano Lett.*, 2016, **16**, 2975-2980.
9. T. Zhao, C. Y. He, S. Y. Ma, K. W. Zhang, X. Y. Peng, G. F. Xie and J. X. Zhong, *J. Phys. Condens. Matter.*, 2015, **27**, 265301.
10. W. H. Han, S. Kim, I. H. Lee and K. J. Chang, *J. Phys. Chem. Lett.*, 2017, **8**, 4627-4632.
11. H. Wang, X. Li, P. Li and J. Yang, *Nanoscale*, 2017, **9**, 850-855.
12. Y. Zhang, Z. F. Wu, P. F. Gao, D. Q. Fang, E. H. Zhang and S. L. Zhang, *Phys. Chem. Chem. Phys.*, 2017, **19**, 2245-2251.
13. P. Li and W. Luo, *Sci. Rep.*, 2016, **6**, 25423.
14. Z. Zhu and D. Tománek, *Phys. Rev. Lett.*, 2014, **112**, 176802.
15. J. L. Zhang, S. Zhao, C. Han, Z. Wang, S. Zhong, S. Sun, R. Guo, X. Zhou, C. D. Gu, K. D. Yuan, Z. Li and W. Chen, *Nano Lett.*, 2016, **16**, 4903-4908.
16. C. Gu, S. Zhao, J. L. Zhang, S. Sun, K. Yuan, Z. Hu, C. Han, Z. Ma, L. Wang, F. Huo, W. Huang, Z. Li and W. Chen, *ACS Nano*, 2017, **11**, 4943-4949.
17. J. Xiao, M. Long, X. Zhang, J. Ouyang, H. Xu and Y. Gao, *Sci. Rep.*, 2015, **5**, 9961.
18. B. Liu, M. Kopf, A. N. Abbas, X. Wang, Q. Guo, Y. Jia, F. Xia, R. Wehrich, F. Bachhuber, F. Pielhofer, H. Wang, R. Dhall, S. B. Cronin, M. Ge, X. Fang, T. Nilges and C. Zhou, *Adv. Mater.*, 2015, **27**, 4423-4429.
19. O. Osters, T. Nilges, F. Bachhuber, F. Pielhofer, R. Wehrich, M. Schoneich and P. Schmidt, *Angew. Chem. Int. Ed. Engl.*, 2012, **51**, 2994-2997.
20. C. Kamal and M. Ezawa, *Phys. Rev. B*, 2015, **91**, 085423
21. D. Kecik, E. Durgun and S. Ciraci, *Phys. Rev. B*, 2016, **94**, 205410.
22. J. Carrete, L. J. Gallego and N. Mingo, *J. Phys. Chem. Lett.*, 2017, **8**, 1375-1380.
23. M. J. Kelly and D. W. Bullett, *Solid State Commun.*, 1976, **18**, 593-595.
24. B. Peng, H. Zhang, H. Shao, K. Xu, G. Ni, J. Li, H. Zhu and C. M. Soukoulis, *J. Mater. Chem. A*, 2018, **6**, 2018-2033.
25. Y. Chen, C. Chen, R. Kealhofer, H. Liu, Z. Yuan, L. Jiang, J. Suh, J. Park, C. Ko, H. S. Choe, J. Avila, M. Zhong, Z. Wei, J. Li, S. Li, H. Gao, Y. Liu, J. Analytis, Q. Xia, M. C. Asensio and J. Wu, *Adv. Mater.*, 2018, **30**, 1800754.
26. F. Ersan, E. Aktürk and S. Ciraci, *Phys. Rev. B*, 2016, **94**, 245417.
27. S. Zhang, M. Xie, F. Li, Z. Yan, Y. Li, E. Kan, W. Liu, Z. Chen and H. Zeng, *Angew. Chem. Int. Ed. Engl.*, 2016, **55**, 1666-1669.
28. S. Ma, P. Zhou, L. Z. Sun and K. W. Zhang, *Phys. Chem. Chem. Phys.*, 2016, **18**, 8723-8729.
29. P. Jamdagni, A. Thakur, A. Kumar, P. K. Ahluwalia and R. Pandey, *Phys. Chem. Chem. Phys.*, 2018, **20**, 29939-29950.
30. H.-S. Tsai, S.-W. Wang, C.-H. Hsiao, C.-W. Chen, H. Ouyang, Y.-L. Chueh, H.-C. Kuo and J.-H. Liang, *Chem. Mater.*, 2016, **28**, 425-429.
31. Z. Zhu, J. Guan and D. Tománek, *Phys. Rev. B*, 2015, **91**, 161404(R).
32. S. Zhang, Z. Yan, Y. Li, Z. Chen and H. Zeng, *Angew. Chem. Int. Ed. Engl.*, 2015, **54**, 3112-3115.
33. M. Amani, E. Regan, J. Bullock, G. H. Ahn and A. Javey, *ACS Nano*, 2017, **11**, 11724-11731.

34. S. Yuan, C. Shen, B. Deng, X. Chen, Q. Guo, Y. Ma, A. Abbas, B. Liu, R. Haiges, C. Ott, T. Nilges, K. Watanabe, T. Taniguchi, O. Sinai, D. Naveh, C. Zhou and F. Xia, *Nano Lett.*, 2018, **18**, 3172-3179.
35. H. Krebs, W. Holz and K. H. Worms, *Ber.*, 1957, **90**, 1031-1037.
36. I. Karakaya and W. T. Thompson, *J. Phase Equilib. Diff.*, 1991, **12**, 343-346.
37. Z. Zhu, J. Guan and D. Tomanek, *Nano Lett.*, 2015, **15**, 6042-6046.
38. M. Xie, S. Zhang, B. Cai, Y. Huang, Y. Zou, B. Guo, Y. Gu and H. Zeng, *Nano Energy*, 2016, **28**, 433-439.
39. F. Shojaei and H. S. Kang, *J. Phys. Chem. C*, 2015, **119**, 20210-20216.
40. Y. Wang, J. Lv, L. Zhu and Y. Ma, *Comput. Phys. Commun.*, 2012, **183**, 2063-2070.
41. Y. Wang, M. Miao, J. Lv, L. Zhu, K. Yin, H. Liu and Y. Ma, *J. Chem. Phys.*, 2012, **137**, 224108.
42. Y. Chen, X. Xi, W.-L. Yim, F. Peng, Y. Wang, H. Wang, Y. Ma, G. Liu, C. Sun, C. Ma, Z. Chen and H. Berger, *J. Phys. Chem. C*, 2013, **117**, 25677-25683.
43. Y. Chen, F. Peng, Y. Yan, Z. Wang, C. Sun and Y. Ma, *J. Phys. Chem. C*, 2013, **117**, 13879-13886.
44. Z. Wang, Y. Li, H. Li, I. Harran, M. Jia, H. Wang, Y. Chen, H. Wang and N. Wu, *J. Alloys Compd.*, 2017, **702**, 132-137.
45. Y. Chen, X. Cai, H. Wang, H. Wang and H. Wang, *Sci. Rep.*, 2018, **8**, 10670.
46. X. Li, H. Li, J. Chen, X. Cai, H. Wang, Z. Lao, B. Sun, L. Tao and Y. Chen, *J. Alloys Compd.*, 2019, **778**, 588-592.
47. I. Harran, Y. Chen, H. Wang, H. Li, Y. Li and L. Tao, *J. Alloys Compd.*, 2017, **710**, 267-273.
48. L. Zhao, W. Yi, J. Botana, F. Gu and M. Miao, *J. Phys. Chem. C*, 2017, **121**, 28520-28526.
49. P. E. Blöchl, *Phys. Rev. B*, 1994, **50**, 17953-17979.
50. G. Kresse and D. Joubert, *Phys. Rev. B*, 1999, **59**, 1758-1775.
51. G. Kresse and J. Furthmüller, *Phys. Rev. B*, 1996, **54**, 11169-11186.
52. M. Dion, H. Rydberg, E. Schröder, D. C. Langreth and B. I. Lundqvist, *Phys. Rev. Lett.*, 2004, **92**, 246401.
53. J. Heyd, G. E. Scuseria and M. Ernzerhof, *J. Chem. Phys.*, 2003, **118**, 8207-8215.
54. A. Togo and I. Tanaka, *Scr. Mater.*, 2015, **108**, 1-5.
55. W. Yu, C.-Y. Niu, Z. Zhu, X. Wang and W.-B. Zhang, *J. Mater. Chem. C*, 2016, **4**, 6581-6587.
56. H. Yin, J. Gao, G.-P. Zheng, Y. Wang and Y. Ma, *J. Phys. Chem. C*, 2017, **121**, 25576-25584.
57. J. Ahn, I. Hong, Y. Kwon, R. C. Clay, L. Shulenburger, H. Shin and A. Benali, *Phys. Rev. B*, 2018, **98**, 085429.
58. A. Ektarawong, S. I. Simak and B. Alling, *Phys. Rev. B*, 2017, **96**, 024202.
59. J. Zeng, P. Cui and Z. Zhang, *Phys. Rev. Lett.*, 2017, **118**, 046101.
60. N. Miao, B. Xu, N. C. Bristowe, J. Zhou and Z. Sun, *J. Am. Chem. Soc.*, 2017, **139**, 11125-11131.
61. F. Zheng, L. Z. Tan, S. Liu and A. M. Rappe, *Nano Lett.*, 2015, **15**, 7794-7800.
62. K. He, C. Poole, K. F. Mak and J. Shan, *Nano Lett.*, 2013, **13**, 2931-2936.
63. L. Seixas, A. S. Rodin, A. Carvalho and A. H. Castro Neto, *Phys. Rev. Lett.*, 2016, **116**, 206803.

64. N. Miao, B. Xu, N. C. Bristowe, J. Zhou, Z. Sun, *JACS* 2017, **139**, 11125-11131.
65. J. Bardeen and W. Shockley, *Phys. Rev.*, 1950, **80**, 72-80.
66. L. Yu and A. Zunger, *Phys. Rev. Lett.*, 2012, **108**, 068701.
67. J. Lv, M. Xu, S. Lin, X. Shao, X. Zhang, Y. Liu, Y. Wang, Z. Chen and Y. Ma, *Nano Energy*, 2018, **51**, 489-495.
68. J. Linghu, T. Yang, Y. Luo, M. Yang, J. Zhou, L. Shen and Y. P. Feng, *Appl. Mater. Interfaces*, 2018, **10**, 32142-32150.
69. M. Bernardi, M. Palummo and J. C. Grossman, *ACS Nano*, 2012, **6**, 10082-10089.
70. M. A. Green, *Prog. Photovoltaics Res. Appl.*, 2017, **25**, 333-334.
71. M. Bernardi, J. Lohrman, P. V. Kumar, A. Kirkeminde, N. Ferralis, J. C. Grossman and S. Ren, *ACS Nano*, 2012, **6**, 8896-8903.
72. L. J. Zhou, Y. F. Zhang and L. M. Wu, *Nano Lett.*, 2013, **13**, 5431-5436.
73. J. Dai and X. C. Zeng, *J. Phys. Chem. Lett.*, 2014, **5**, 1289-1293.
74. N. Lu, H. Guo, L. Wang, X. Wu and X. C. Zeng, *Nanoscale*, 2014, **6**, 4566-4571.

TOC Figure:

